# Investigation of Supersonic Wakes Using Conventional and Hybrid Turbulence Models

Richard D. Sandberg* and Hermann F. Fasel[†]

*The University of Arizona, Tucson, Arizona 85721*

Transitional and turbulent supersonic wakes behind axisymmetric bodies with a blunt base are investigated numerically using state-of-the-art Reynolds averaged Navier–Stokes models and the flow simulation methodology. The centerpiece of the flow simulation methodology is a strategy to provide the proper amount of modeling of the subgrid scales. This is accomplished by a "contribution function" which locally and instantaneously compares the smallest relevant scales to the local grid size. The turbulence closures chosen are a state-of-the-art wall-distance free explicit algebraic stress model, or a standard $K$–$\epsilon$ model for comparison. Axisymmetric Reynolds averaged Navier–Stokes and fully three-dimensional flow simulation methodology calculations are performed on various computational grids for wakes at $M = 2.46$ for several Reynolds numbers. The data obtained from all simulation strategies are compared with available direct numerical simulation results for the transitional cases and to experimental results at the highest Reynolds number investigated. Of particular interest is the performance of commonly used compressibility corrections and modifications to closure-coefficients specifically derived for high-Reynolds number flows. The ability of the flow simulation methodology to reproduce flow structures found in direct numerical simulations is scrutinized and a reason for the failure of Reynolds averaged Navier–Stokes calculations to correctly predict the base pressure-distribution is given.

## Nomenclature

| | | |
|---|---|---|
| $a, c, C$ | = | constants |
| $c_p$ | = | pressure coefficient |
| $c_T$ | = | constant for wall-damping function |
| $c_v$ | = | specific heat |
| dt | = | computational time step |
| $E$ | = | total energy, $c_v T + \frac{1}{2} u_i u_i$ |
| $f(\Delta/L_K)$ | = | contribution function |
| $f_{\epsilon2}, f_\mu$ | = | wall-damping functions |
| $K$ | = | turbulent kinetic energy |
| $k$ | = | azimuthal Fourier mode number |
| $L_K$ | = | Kolmogorov length scale |
| $M, M_T$ | = | Mach number, turbulent Mach number |
| $N$ | = | wall distance |
| nr | = | number of radial grid points |
| nz | = | number of streamwise grid points |
| $Pr, Pr_T$ | = | Prandtl number, turbulent Prandtl number |
| $p$ | = | pressure |
| $p, q, r, \phi$ | = | coefficients for $\mathrm{EASM}_\alpha$ |
| $q_k, Q_k$ | = | heat-flux vector, turbulent heat-flux vector |
| $Re, Re_T$ | = | Reynolds number, turbulent Reynolds number |
| $S_{ik}$ | = | strain-rate tensor |
| $T$ | = | temperature |
| $t$ | = | time |
| $u, v, w$ | = | velocity components in the streamwise, radial, and azimuthal direction |
| $\langle u_i' u_k' \rangle$ | = | turbulent stress tensor |
| $W_{ik}$ | = | vorticity tensor |
| $x_k$ | = | coordinate |
| $z, r, \theta$ | = | streamwise, radial, and azimuthal coordinate |
| $\beta$ | = | parameter in contribution function |
| $\gamma$ | = | ratio of specific heats |
| $\gamma^*$ | = | coefficients for $\mathrm{EASM}_\alpha$ |
| $\Delta$ | = | computational grid size |
| $\delta_{ik}$ | = | Kronecker operator |
| $\epsilon$ | = | turbulent dissipation rate |
| $\mu, \mu_T$ | = | molecular, turbulent viscosity |
| $\nu_T$ | = | turbulent kinematic viscosity |
| $\Pi$ | = | source term |
| $\sigma_\epsilon, \sigma_K, \sigma_\rho$ | = | constants for turbulent transport equations |
| $\tau_{ik}$ | = | molecular stress tensor |
| $\tau_T$ | = | turbulent time scale, $K/\epsilon$ |

*Subscripts*

| | | |
|---|---|---|
| $c$ | = | base corner |
| $D$ | = | quantity based on diameter of cylinder |
| $\epsilon$ | = | transport equation for turbulent dissipation rate |
| $i, j, k, l$ | = | indices for Cartesian tensor notation |
| $K$ | = | transport equation for turbulent kinetic energy |
| max | = | maximum of referring quantity |
| $T$ | = | turbulent |

*Superscripts*

| | | |
|---|---|---|
| $R$ | = | quantity obtained from RANS closure |
| $-$ | = | Reynolds average |
| $'$ | = | fluctuation quantities for Reynolds average |
| $\sim$ | = | Favre average, filtered variable |
| $''$ | = | fluctuation quantities for Favre average |
| $*$ | = | quantity for $\mathrm{EASM}_\alpha$ |
| $+$ | = | wall coordinates |

*Presently Research Fellow, School of Engineering Sciences, University of Southampton, Southampton SO17 1BJ England, United Kingdom; sandberg@soton.ac.uk. Member AIAA.

[†]Professor, Department of Aerospace and Mechanical Engineering; faselh@email.arizona.edu. Member AIAA.

## I.  Introduction

VARIOUS axisymmetric bodies at supersonic speeds, such as missiles, rockets, or projectiles, present a blunt base to the flow. A recirculation region forms behind the base of the body that is responsible for a low base pressure, thus causing aerodynamic drag (base drag). In-flight base pressure measurements with projectiles (U.S. Army 549 projectile) have shown that the base drag may account for up to 35% of the total drag [1]. The total drag determines the range, terminal velocity, or the payload of the object, thus playing

a crucial role in the design process. Because of the large contribution of the base drag to the overall drag, bluff bodies in supersonic flow have been the target of many previous research efforts, both experimental and computational.

Extensive experimental investigations of supersonic axisymmetric base flows have been performed at the University of Illinois at Urbana–Champaign (UIUC) [2,3]. Planar visualizations [4] revealed that large-scale structures are present in the flow which may have a significant impact on the mean flow and, hence, the mean base pressure. Even though large structures were shown to exist, their origin and impact on the mean flow was far from understood. However, considering that a drag reduction was achieved by reducing the intensity of turbulent structures [5], it seems that the key to uncovering the essential mechanisms for drag reduction is to first understand the role of large structures. Only then can it be determined how the dynamics of these structures is modified by techniques for drag reduction. Unfortunately the high speeds of the flows make it very difficult to experimentally acquire time dependent data with the necessary temporal resolution to track individual structures and get clues about their origin and evolution. Therefore, complementary numerical simulations might offer valuable insights into the physical mechanisms relevant in the near-wake region. Direct numerical simulations (DNS) of transitional wakes confirmed the occurrence of large-scale structures with a pronounced effect on the base drag [6]. However, DNS of wakes at Reynolds numbers on the order of $\mathcal{O}(10^6)$, as in the experiments at UIUC, with sufficient resolution in all three dimensions and in time are out of reach even with present supercomputers. Even fully resolved DNS of transitional wakes [6,7] are computationally very expensive. Therefore, other approaches for computing such flows have to be considered, such as Reynolds averaged Navier–Stokes equations (RANS) and large eddy simulation (LES).

Because of much less restricting resolution requirements in comparison to DNS, RANS calculations have been the method of choice in the past. Several attempts have been made to use RANS for calculating supersonic base flows. Sahu et al. [8] were among the first to compute the flow around an entire projectile using the thin-layer Navier–Stokes equations and an algebraic eddy viscosity (zero equation) model. Sahu [9] compared the results of different RANS models and found that the pressure distribution on the base showed a strong peak at the center, something not seen in the experiments even though the magnitude of the average pressure over the base was predicted within a few percent. In the hope that neglecting compressibility effects had been the reason for failure of earlier efforts, further studies [10,11] incorporated compressible extensions to account for the influence of dilatational terms [12,13] and showed some improvement over previous results. However, they found that the eddy viscosity in the recirculation region and the $K$-level in the shear layer was overpredicted, resulting in too short a recirculation length. The aforementioned deficiencies in the results obtained from RANS calculations might be attributed to the lack of capturing the effect of the unsteady flow structures on the mean flow. That this is indeed the case will be shown in the present paper.

Therefore, for the flow under consideration, LES might seem like the method of choice because of the ability to capture three-dimensional and unsteady flow structures and has been used for the base flow problem by Fureby [14], for example. In addition to several shortcomings of the "standard" Smagorinsky LES model [15,16], the resolution requirements for the wall-bounded flow region for large Reynolds numbers are still severe.

To further reduce computational costs while still computing unsteady flows with large coherent structures, hybrid RANS/LES approaches have been proposed. The underlying principle is to conduct RANS-type calculations close to walls and perform LES away from walls to capture the dominant unsteady flow structures. One way of implementing this approach is known as detached eddy simulation (DES) [17] and has been applied to the UIUC experiments [18,19].

In the present investigation, a different approach is considered, namely the flow simulation methodology (FSM) [20–23]. The centerpiece of FSM is a strategy to provide a proper amount of modeling of the subgrid scales based on the "local and time-instantaneous physical resolution" of the calculation. This is accomplished by employing a so-called contribution function, which locally and instantaneously compares the smallest relevant turbulent flow scales to the local computational grid size. The contribution function has to be designed such that it provides no modeling if the computation is locally well resolved so that the computation approaches a DNS in the fine-grid limit, or provides modeling of all scales in the coarse-grid limit and thus approaches a RANS or unsteady RANS (URANS) calculation. In between these resolution limits, the contribution function adjusts the necessary modeling for the unresolved scales whereas the larger (resolved) scales are computed as in traditional LES. However, in contrast to traditional LES, the subgrid scales are now modeled using a two-equation turbulence model.

The objective of this paper is to apply RANS calculations and the FSM to transitional and turbulent supersonic base flows. Transitional wakes were considered for several reasons: firstly, to evaluate whether the approach is able to represent a transitional flow in general. Capturing the laminar-turbulent transition is a tough task for any flow simulation strategy, as the additional dissipation from turbulence models frequently inhibits or significantly delays the mechanisms leading to transition. Secondly, a vast amount of data were available from DNS [6], such that a detailed comparison between FSM results and DNS data could be made. In particular it will be investigated whether FSM can capture the same flow structures and if the same dominant modes as those found in DNS are predicted. The dominant modes and the associated structures have been shown strongly affect mean flow quantities, in particular the base pressure [6,7]. It will be shown that the failure to capture the aforementioned structures using RANS calculations might explain the discrepancies in the mean flow quantities when compared with DNS data or experiments. In contrast, using FSM in combination with a state-of-the-art turbulence model and fully three-dimensional distributions of turbulent quantities should capture the relevant unsteady large structures. This might lead to better prediction of the mean flow quantities in the near-wake region and, in particular, to a more accurate determination of the base-pressure than possible with steady RANS.

## II.  Governing Equations

The fluid is assumed to be an ideal gas with constant specific heat coefficients. All quantities are made dimensionless using the flow quantities at a reference location in the flow, here the freestream/inflow location. The radius of the body was chosen as the reference length. The nondimensional equations for the resolved continuity, momentum, and the energy equations are

$$\frac{\partial \bar{\rho}}{\partial t} + \frac{\partial}{\partial x_k}(\bar{\rho}\tilde{u}_k) = 0$$

$$\frac{\partial}{\partial t}(\bar{\rho}\tilde{u}_i) + \frac{\partial}{\partial x_k}[\bar{\rho}\tilde{u}_i\tilde{u}_k + \bar{p}\delta_{ik} - (\bar{\tau}_{ik} - \bar{\rho}\sigma_{ik})] = 0, \quad (1)$$

$$\frac{\partial}{\partial t}(\bar{\rho}E_R) + \frac{\partial}{\partial x_k}\left[\bar{\rho}\tilde{u}_k\left(E_R + \frac{\bar{p}}{\bar{\rho}}\right) + \bar{q}_k + Q_k - \tilde{u}_i(\bar{\tau}_{ik} - \bar{\rho}\sigma_{ik})\right] = \Pi$$

with the resolved total energy being defined as $E_R = c_v\tilde{T} + \frac{1}{2}\tilde{u}_i\tilde{u}_i$. The resolved stress tensor and the resolved heat-flux vector are computed as

$$\bar{\tau}_{ik} = \frac{2\bar{\mu}}{Re}\left(\tilde{S}_{ik} - \frac{1}{3}\tilde{S}_{jj}\delta_{ik}\right), \qquad q_k = \frac{-\mu}{(\gamma-1)M^2 PrRe}\frac{\partial T}{\partial x_k} \quad (2)$$

respectively, where the Prandtl number is assumed to be constant at $Pr = 0.70$, and $\gamma = 1.4$. To close the system of equations, the pressure is obtained from the nondimensional equation of state $\bar{p} = (\bar{\rho}\tilde{T})/(\gamma M^2)$.

The preceding equations contain three terms that require modeling: the subgrid stress tensor $\sigma_{ik}$, the subgrid heat-flux vector

$Q_k$, and the source term $\Pi$ in the energy equation. For DNS, where it is assumed that all relevant time and length scales are resolved by the computational grid, the model terms are zero, thus $\phi = \bar{\phi} = \tilde{\phi}$. In the other limit, where all fluctuations are averaged out, a traditional RANS is recovered.

For modeling of the unresolved scales, turbulence models are employed that require knowledge of the turbulent kinetic energy $K$ and the turbulent dissipation rate $\epsilon$. They are computed solving two additional compressible transport equations [21]:

$$\frac{\partial}{\partial t}(\bar{\rho}K) + \frac{\partial}{\partial x_k}\left[\bar{\rho}\tilde{u}_k K - \left(\frac{\bar{\mu}}{Re} + \frac{\mu_T}{\sigma_K}\right)\frac{\partial K}{\partial x_k}\right] = \Pi_K \qquad (3)$$

$$\frac{\partial}{\partial t}(\bar{\rho}\epsilon) + \frac{\partial}{\partial x_k}\left[\bar{\rho}\tilde{u}_k \epsilon - \left(\frac{\bar{\mu}}{Re} + \frac{\mu_T}{\sigma_\epsilon}\right)\frac{\partial \epsilon}{\partial x_k}\right] = \Pi_\epsilon \qquad (4)$$

The diffusion terms of the $K$- and the $\epsilon$-equations include the turbulent viscosity which is given as $\mu_T = c_\mu \bar{\rho} K \tau_T$ with $c_\mu = 0.09$. Additional constants for the diffusion terms are $\sigma_K = 1.0$ and $\sigma_\epsilon = 1.3$.

## A. Source Terms

The source terms on the right-hand side of the transport Eqs. (1), (3), and (4) include compressible extensions employing the models of Sarkar [13] for the pressure dilatation and of Speziale [15] for the turbulent mass fluxes:

$$\Pi^R = (1 - a_2 M_T)\bar{\rho}\sigma_{ik}\tilde{S}_{ik} + (1 - a_3 M_T^2)\bar{\rho}\epsilon$$
$$+ (\bar{\tau}_{ik} - \bar{\rho}\delta_{ik})\frac{\partial}{\partial x_k}\left[\frac{C_\mu}{\bar{\rho}\sigma_p}\tau_T K \frac{\partial \bar{\rho}}{\partial x_i}\right] \qquad (5)$$

$$\Pi_K = -(1 - a_2 M_T)\bar{\rho}\sigma_{ik}\tilde{S}_{ik} - (1 - a_3 M_T^2)\bar{\rho}\epsilon$$
$$- \left(\frac{\partial p}{\partial x_i} - \frac{\partial \tau_{ik}}{\partial x_k}\right)\frac{C_\mu}{\bar{\rho}\sigma_p}\tau_T K \frac{\partial \bar{\rho}}{\partial x_i} \qquad (6)$$

$$\Pi_\epsilon = -C_{\epsilon 1}\bar{\rho}\frac{1}{\tau_T}\sigma_{ik}\left(\frac{\partial \tilde{u}_i}{\partial x_k} - \frac{1}{3}\frac{\partial \tilde{u}_i}{\partial x_j}\delta_{ik}\right) - C_{\epsilon 2}f_{\epsilon 2}\bar{\rho}\frac{\epsilon}{\tau_T}$$
$$+ C_{\epsilon 3}\bar{\rho} Re_T^{\frac{1}{2}}\frac{\epsilon}{\tau_T} - \frac{4}{3}\bar{\rho}\epsilon\frac{\partial \tilde{u}_j}{\partial x_j} \qquad (7)$$

with $\sigma_\rho = 0.5$, $C_{\epsilon 1} = 1.44$, $C_{\epsilon 2} = 1.83$, and $C_{\epsilon 3} = 0.001$:

$$M_T = \sqrt{\frac{2K}{\tilde{T}}}M, \qquad Re_T = \frac{\rho K}{\mu}\tau_T \qquad (8)$$

To remove singularities at walls, i.e., $K = 0$, in the destruction term of the $\epsilon$-equation, traditionally a damping function of the form $f_{\epsilon 2}(N) = 1 - \exp(-Re\sqrt{0.1K}N)$ is used. In the EASM$_\alpha$ (described next), this wall-damping function is the only term containing a wall distance; the Reynolds stress model automatically accounts for near-wall effects through the computation of $\alpha_1/\tau_T$ [see Eq. (13)]. To be completely independent of the wall distance, another approach is used for computing $f_{\epsilon 2}$. It is based on the assumption that the smallest physical time-scale in a turbulent flow is the Kolmogorov time-scale. Therefore, by computing $f_{\epsilon 2}$ as

$$f_{\epsilon 2} = \frac{1}{\max[1, c_T/\sqrt{Re_T}]} \qquad (9)$$

a completely wall distance independent model is obtained. This function contains an additional constant $c_T$ that requires calibration.

## B. Turbulent Stress Tensor

For the closure of the turbulent stress tensor $\sigma_{ik}$, two different models were used.

*1. Standard K-ε Model (STKE)*

The subgrid stress tensor is computed from

$$\sigma_{ik}^R = \frac{2}{3}K\delta_{ik} - 2c_\mu f_\mu \tau_T K\left(\tilde{S}_{ik} - \frac{1}{3}\frac{\partial u_j}{\partial x_j}\delta_{ik}\right) \qquad (10)$$

with the wall-damping function $f_\mu = 1 - \exp(-N^+/26)$, where $N^+$ is the wall-normal distance.

*2. Explicit Algebraic Stress Model (EASM$_\alpha$)*

The flow under investigation features physically very disparate regions such as a boundary layer, a free shear layer subject to pressure gradients, and a recirculation region. It is safe to say that assuming the production to dissipation ratio to be a constant cannot hold for all regions. For that reason, the EASM$_\alpha$, presented in Rumsey et al. [24], was chosen. The Reynolds stress model is based on the original EASM by Gatski and Speziale [25] which was used for our previous investigations [23,26]. The stress tensor is computed from

$$\sigma_{ik}^R = \frac{2}{3}K\delta_{ik} - 2v_t^*\left[\left(\tilde{S}_{ik} - \frac{1}{3}\frac{\partial u_j}{\partial x_j}\delta_{ik}\right) + a_2 a_4(\tilde{S}_{ij}\tilde{W}_{jk} + \tilde{S}_{kj}\tilde{W}_{ji})\right]$$
$$- 2a_3 a_4\left(\tilde{S}_{ij}\tilde{S}_{jk} - \frac{1}{3}\tilde{S}_{jl}\tilde{S}_{jl}\delta_{ik}\right)\right] \qquad (11)$$

with $\tilde{W}_{ik} = \frac{1}{2}(\partial \tilde{u}_i/\partial x_k - \partial \tilde{u}_k/\partial x_i)$. The kinematic eddy viscosity is given by

$$v_t^* = C_\mu^* K\tau_T = -K\tau_T\left(\frac{\alpha_1}{\tau_T}\right) \qquad (12)$$

The value of $\alpha_1/\tau_T$ is obtained by locally and instantaneously solving the following cubic equation:

$$\left(\frac{\alpha_1}{\tau_T}\right)^3 + p\left(\frac{\alpha_1}{\tau_T}\right)^2 + q\left(\frac{\alpha_1}{\tau_T}\right) + r = 0 \qquad (13)$$

where

$$p = -\frac{\gamma_1^*}{\phi\gamma_0^*}, \qquad r = \frac{\gamma_1^* a_1}{(2\phi\gamma_0^*)^2}$$
$$q = \frac{1}{(2\phi\gamma_0^*)^2}\left(\gamma_1^{*2} - 2\phi\gamma_0^* a_1 - \frac{2}{3}\phi a_3^2 - 2W^2 \tau_T^2 a_2^2\right)$$

The needed parameters are assembled as follows:

$$\phi = \tilde{S}_{ik}\tilde{S}_{ik}\tau_T^2, \qquad W^2 = -\tilde{W}_{ik}\tilde{W}_{ik}, \qquad a_4 = \frac{\tau_T}{\gamma_1^* - 2\gamma_0^*(\alpha_1/\tau_T)\phi}$$
$$\gamma_0^* = \frac{C_1^1}{2}, \qquad \gamma_1^* = \frac{C_1^0}{2} + \left(\frac{C_{\epsilon 2} - C_{\epsilon 1}}{C_{\epsilon 1} - 1}\right) \qquad (14)$$

The constants are given as $C_1^0 = 3.4$, $C_1^1 = 1.8$, $a_1 = 0.4866$, $a_2 = 0.8$, and $a_3 = 0.375$. An algorithm to solve the cubic equation is given in detail in Rumsey and Gatski [27]. Hence, the turbulent viscosity for the most recent EASM$_\alpha$ is computed without having to assume a ratio of turbulent production over turbulent dissipation, in contrast to the original EASM [25].

## C. Turbulent Heat-Flux Vector

The turbulent heat-flux vector $Q_k$ is modeled according to Speziale [15]

$$Q_k^R = -\frac{1}{\gamma(\gamma - 1)M^2}\frac{\mu_T}{Pr_T}\frac{\partial \tilde{T}}{\partial x_k}$$

with $Pr_T = 0.9$.

## III. Flow Simulation Methodology

For the flow simulation methodology, the turbulent stress tensor is multiplied by the contribution function $f(\Delta/L)$

$$\sigma_{ik} = f(\Delta/L)\sigma_{ik}^R \qquad (15)$$

For the compressible extension, the source term in the energy equation and the turbulent heat-flux vector also have to be rescaled with the contribution function

$$Q_k = f(\Delta/L)Q_k^R \quad \text{and} \quad \Pi = f(\Delta/L)\Pi^R \qquad (16)$$

The term $\Delta = [(\Delta z^2 + \Delta r^2 + (r\Delta\theta)^2)/3]^{1/2}$ is the representative computational grid size and $L$ is the relevant length-scale. In the present calculations we have used a contribution function in a form proposed by Speziale [21]

$$f(\Delta/L_k) = (1 - e^{-\beta\frac{\Delta}{L_k}})^n \qquad (17)$$

where $L_K = \nu^{3/4}/\epsilon^{1/4}$ and where $\beta$ and $n$ are parameters requiring calibration. Currently $n$ is set to unity and $\beta$ is set to a small value in the order of $\mathcal{O}(10^{-3})$. Other forms of the contribution function and different choices of the length-scale are possible [22].

## IV.  Numerical Method

The compressible Navier–Stokes equations and the fully three-dimensional transport equations for $K$ and $\epsilon$ in cylindrical coordinates are solved using sixth-order accurate split compact differences for the radial direction, fourth-order accurate split differences in the streamwise direction, and a pseudospectral discretization in the azimuthal direction. To preserve accuracy, the finite differences are derived for nonequidistant computational grids. The computational domain is shown in Fig. 1. Region 1 covers the approach boundary layer up to the base corner and region 2 extends from the trailing edge to the outflow boundary. A domain decomposition is employed in the streamwise direction to perform computations on parallel computers with the interface between region 1 and 2 always being a CPU boundary. Communication between adjacent subdomains enables the use of the same finite difference stencils across the CPU boundaries as in the interior of each subdomain to maintain high-order accuracy. Shock waves are captured properly by employing split forward/backward finite differences, similar to the method given in Gottlieb and Turkel [28], albeit applied to the compressible Navier–Stokes equations. This ensures that the overall high accuracy of the solution is maintained. A state-of-the-art axis treatment is implemented, exploiting parity conditions [6]. For the time advancement, a standard fourth-order Runge–Kutta scheme is employed.

The use of a high-order numerical method for the evaluation of the Reynolds stress tensor and the turbulence transport equations allows for a better separation of the contribution of the turbulence model



Fig. 1   **Computational domain.**

from the truncation error of the numerical scheme than would be possible with lower order accurate schemes. Further details on the numerical procedure and a thorough validation are given in Sandberg [29].

## V.  Results

The same code was used for both RANS and FSM calculations. To conduct RANS calculations, the contribution function $f(\Delta/L_k)$ was set to unity, therefore using the subgrid quantities computed with the specified turbulence closure in an unmodified way. When conducting FSM calculations, the contribution function was computed as specified in Eq. (17).

### A.  Transitional Wakes

For all transitional cases, it was assumed that the approach flow is laminar. Therefore, the contribution function was manually set to zero in the approach flow, such that no model was employed and the boundary layer remained laminar. In addition, $K$ was set to zero at the inflow boundary to be consistent with the laminar approach-flow assumption.

#### 1.  Axisymmetric RANS Calculations

Axisymmetric RANS calculations were conducted, employing the standard $K$-$\epsilon$ model (STKE) and the generalized version of the explicit algebraic stress model EASM$_\alpha$ [24]. The closures were employed using either the traditional wall-damping function [henceforth referred to as $f_{\epsilon2}(N)$], or the wall-distance independent wall-damping function given in (9). In light of validation calculations at moderate Reynolds numbers [29,30], the constant $c_T$ contained in the wall-distance independent wall-damping function was set to either $c_T = 4.56$ or $c_T = 4.65$. Calculations using the wall-distance independent approach are referred to as $c_T = $ constant used. Two separate computational grids were used. The coarse grid had $162 \times 90$ points in the streamwise and the radial direction, respectively, with the smallest grid spacing $\Delta r_c = \Delta z_c = 0.02R$ at the corner. The fine computational grid had $302 \times 130$ points in the streamwise and the radial directions, respectively, and the finest spacing at the corner of the body was $\Delta r_c = \Delta z_c = 0.01R$.

Figure 2 shows the streamwise centerline velocity and the radial distributions of the pressure coefficient on the base for $Re_D = 6 \times 10^4$. For reference, DNS results [6] are included. All axisymmetric RANS calculations underpredict the recirculation length significantly, and, consequently, also predict too low a pressure on the base. The pressure distribution on the base also shows a considerable radial variation, albeit with different strength for different models. The calculation employing the STKE model yields the shortest recirculation length and the lowest pressure value with the strongest radial variation. This is most likely due to the overprediction of the eddy viscosity in the shear layer and within the recirculation region.

When looking at the streamwise axis-velocity distribution, the data obtained from calculations employing the EASM$_\alpha$ with $f_{\epsilon2}(N)$, $c_T = 4.56$ or $c_T = 4.65$ practically collapse onto one curve, independent of the computational grid that was used. However, the recirculation length is still significantly underpredicted. This is likely caused by the large values of $K$ close to the base and in the initial shear layer, as the model mistakes this laminar region for a turbulent region.

Only when scrutinizing the base pressure, a difference between the coarse and the fine computational grid becomes visible. For the fine grid, $c_p$ is slightly larger than for the coarse grid. Nevertheless, the data of calculations using $f_{\epsilon2}(N)$ or $c_T = 4.56$ coincide for both grids. Overall, the values found for $c_T$ with calibration calculations of turbulent boundary layers appear to be transferrable to the base flow case. It is noteworthy that, for the wake, the global solution is less sensitive to the value of $c_T$ than for the turbulent boundary layer.

Overall, the EASM$_\alpha$ appears to be the better-suited model for the flow under consideration, showing a recirculation length and a base pressure closest to the DNS results, due to appropriately reduced
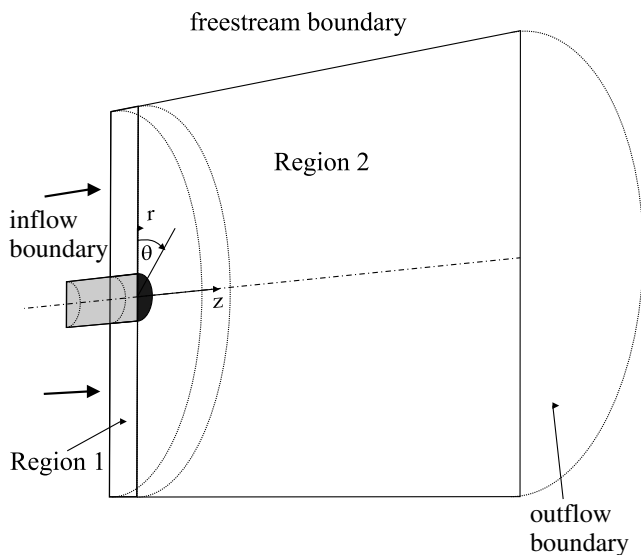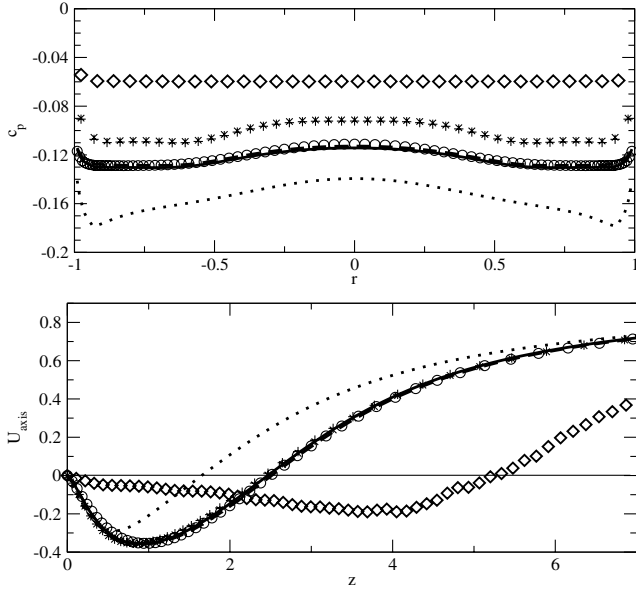
a) DNS, $k_{max} = 128$

b) FSM, fine grid, $k_{max} = 16$, $\beta = 1 \times 10^{-3}$

c) FSM, coarse grid, $k_{max} = 4$, $\beta = 2 \times 10^{-4}$

d) FSM, coarse grid, $k_{max} = 4$, $\beta = 1 \times 10^{-3}$

Fig. 3 Side views of contours of instantaneous vorticity magnitude; $Re_D = 6 \times 10^4$, $M = 2.46$.

Fig. 2 Base pressure coefficient (top) and streamwise axis velocity (bottom); DNS, $k_{max} = 128$ ($\diamond$), coarse grid $f_{\epsilon2}(N)$ (solid curve), coarse grid $c_T = 4.56$ (dashed curve), coarse grid $c_T = 4.65$ ($\bigcirc$), coarse grid $f_{\epsilon2}(N)$, STKE model (dotted curve), fine grid $f_{\epsilon2}(N)$ (+), fine grid $c_T = 4.56$ (×); $Re_D = 6 \times 10^4$, $M = 2.46$.

levels of turbulent production. Nevertheless, even the most successful RANS calculation is far from reproducing the physically correct flat base pressure distribution and streamwise axis-velocity distribution of the DNS. It is therefore suggested that to correctly predict supersonic base flows, the unsteady structures need to be included in the simulations.

### 2. 3-D FSM Calculations

For the FSM calculations, only the EASM$_\alpha$ was employed as it produced superior axisymmetric RANS results. As has previously been shown [23,26], the FSM obtains similar results independent of the turbulence closure used. Nevertheless, it is expected that a better closure can help reduce computational costs even further and yield reasonable results for coarser computational grids. As initial condition for the FSM calculations, the axisymmetric RANS data was used and the desired number of azimuthal Fourier modes was added, initialized to zero. The flow was then initially pulsed in the higher Fourier modes of density to achieve faster development of three-dimensionality. From the experience with a lower Reynolds number transitional wake [23,26] and following the suggestion by Speziale [20], the value of the constant $\beta$ in the contribution function (17) was initially set to $\beta = 2 \times 10^{-3}$ and then varied.

Figures 3a–3d show sideviews of instantaneous vorticity magnitude for FSM calculations on both computational grids with different values of $\beta$ compared with DNS data. The DNS calculation displays a broad range of scales. For the FSM calculation on the fine grid and the FSM using the coarse grid with $\beta = 2 \times 10^{-4}$, the small-scale structures vanish and only some large-scale structures (on the order of the shear layer thickness) are resolved on the respective computational grid. The values of the time-averaged contribution functions of these two cases are shown in Fig. 4a and 4b for the plane $\theta = 0$ deg. Clearly, the largest contribution of the turbulence model is provided in the shear layer, reaching values of up to 5% downstream of recompression. The very low value of $f(\Delta/L_K)$ within the recirculation region and the initial shear layer allows for the formation of structures.

Increasing $\beta$ to $1 \times 10^{-3}$ on the coarse grid leads to much higher values of the contribution function, as can be seen in Fig. 4c. The distribution of $f(\Delta/L_K)$ is very similar to the other cases; however, the absolute values are significantly larger, with a maximum of $f(\Delta/L_K) > 10\%$ downstream of recompression. This results in the complete removal of structures, as can be seen in Fig. 3d, and only a
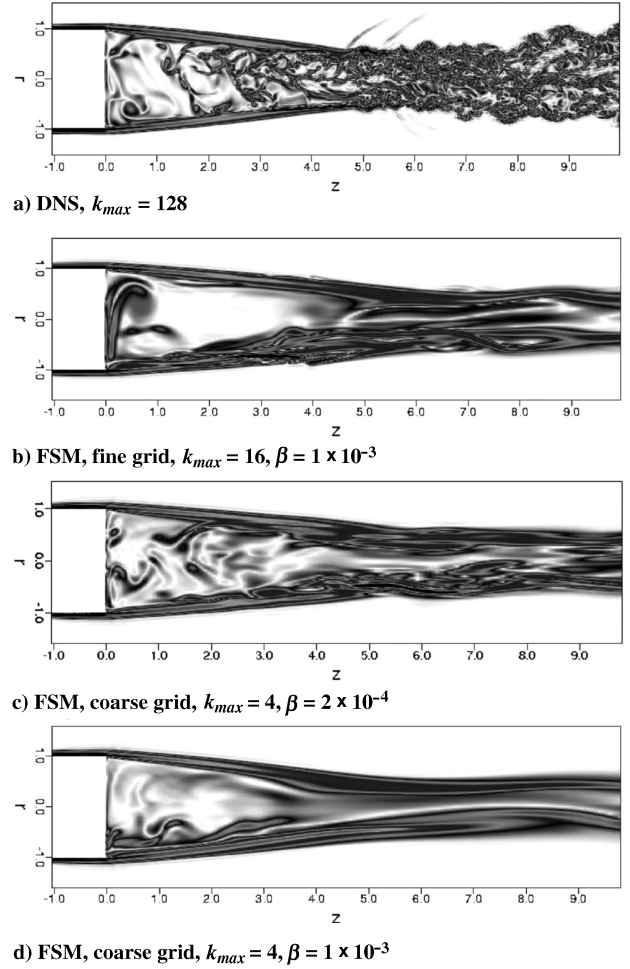
flapping motion of the flow remains, implying that the calculation approaches the URANS-limit of the FSM strategy.

The preceding results show that similar shapes and values of the contribution function can be obtained with either very coarse grids, using a small value of $\beta$, or using finer grids with larger values of $\beta$. For a more quantitative evaluation of the performance of the FSM on different computational grids and varying $\beta$, the time-averaged streamwise velocity along the axis of symmetry and the time-averaged pressure coefficient on the base are examined.

First, the results obtained on a fixed computational grid with varying $\beta$ are shown in Fig. 5. The DNS data and the axisymmetric RANS calculation used as initial condition are included for reference. In contrast to the axisymmetric RANS calculations, the pressure distribution obtained by all FSM computations is practically flat, with the magnitude close to the value predicted with DNS. That even FSM calculations with $k_{max} = 4$ predict a flat base pressure confirms that this observation can be attributed to the unsteadiness caused by azimuthal modes with low wavenumbers [6]. The best agreement between an FSM calculation and DNS is achieved by setting $\beta = 1 \times 10^{-3}$ or $\beta = 2 \times 10^{-3}$. For smaller values of $\beta$, the predicted recirculation region is too long. Keeping $\beta$ constant at $4 \times 10^{-3}$ and increasing the number of azimuthal Fourier modes, $k_{max}$, from 4 to 8 on the coarse computational grid only marginally affects the solution. However, when using $k_{max} = 16$ with the same computational grid and $\beta = 4 \times 10^{-3}$, the recirculation length is overpredicted, and, as a consequence, so is the base pressure. In fact, the results resemble the data obtained with four azimuthal Fourier modes using $\beta = 2 \times 10^{-4}$. Increasing the resolution, here the number of Fourier modes, has the same effect as decreasing $\beta$: it leads to smaller values of the contribution function. Consequently, a larger amount of structures has to be resolved by the grid to reproduce
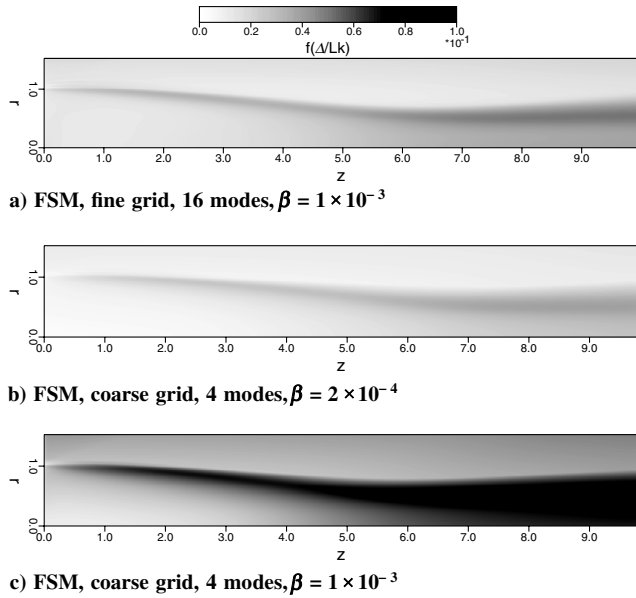
a) FSM, fine grid, 16 modes, $\beta = 1 \times 10^{-3}$



b) FSM, coarse grid, 4 modes, $\beta = 2 \times 10^{-4}$



c) FSM, coarse grid, 4 modes, $\beta = 1 \times 10^{-3}$

Fig. 4   Time-averaged contribution function $f(\Delta/L_K)$ for FSM; $Re_D = 6 \times 10^4$, $M = 2.46$.
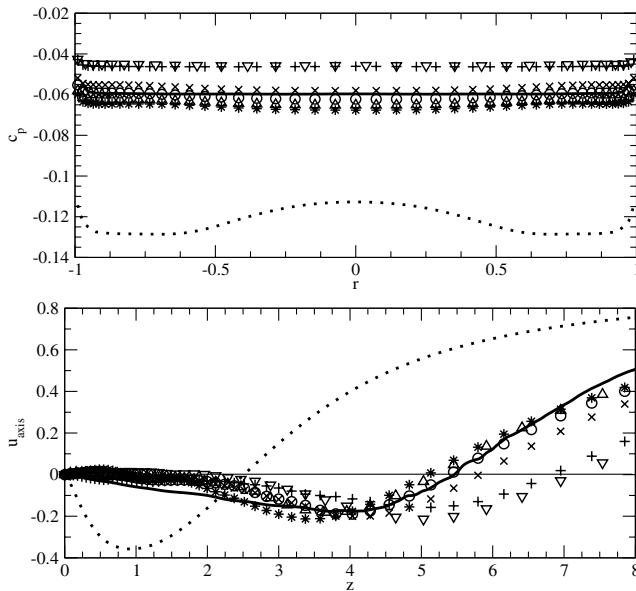


Fig. 5   Time-averaged pressure coefficient (top) and streamwise axis-velocity (bottom) for FSM on coarse grid with $k_{\max} = 4$ unless noted otherwise; DNS, $k_{\max} = 128$ (solid curve), axisymmetric RANS (dotted curve), $\beta = 2 \times 10^{-4}$ (+), $\beta = 1 \times 10^{-3}$ (×), $\beta = 2 \times 10^{-3}$ (○), $\beta = 4 \times 10^{-3}$ (*), $\beta = 4 \times 10^{-3}$ and $k_{\max} = 8$ (△), $\beta = 4 \times 10^{-3}$ and $k_{\max} = 16$ (▽); $Re_D = 6 \times 10^4$, $M = 2.46$.
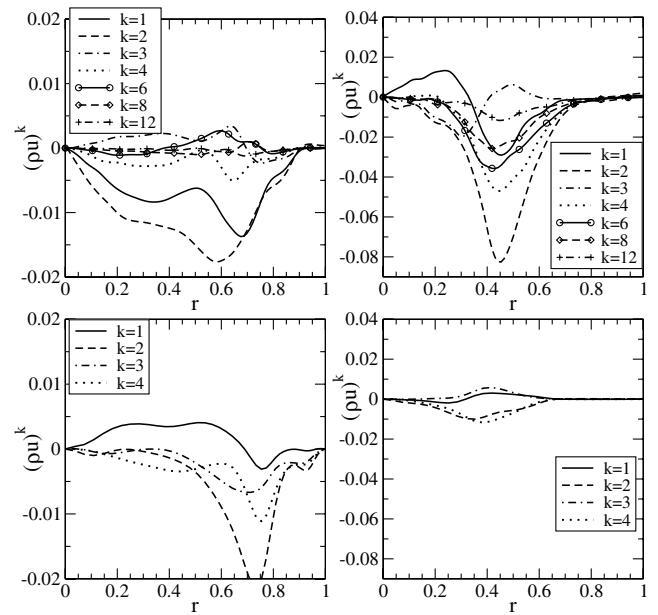


Fig. 6   Time-averaged mode shapes of $(\rho u)^k$; DNS (top) and FSM calculation on coarse grid with $k_{\max} = 4$ and $\beta = 2 \times 10^{-4}$ (bottom); $z = 2.5$ (left) and $z = 7$ (right); $Re_D = 6 \times 10^4$, $M = 2.46$.

a physically correct flow field. The streamwise/radial grid, however, apparently is too coarse to capture all relevant structures that are not accounted for by the proper amount of turbulence model. In other words, the contribution from the turbulence model is too small to dissipate the scales that cannot be resolved on the computational grid.

This can be confirmed by looking at the time-averaged radial amplitude distributions of the azimuthal Fourier modes obtained from the FSM calculation on the coarse grid, using too small a value of $\beta$ shown in Fig. 6. The azimuthal Fourier modes of the streamwise velocity component are chosen as they contain most of the energy. At the upstream location, as a result of the small values of the contribution function in this region, the magnitudes of all modes correspond roughly to those found in DNS (shown on top). However, mode $k = 4$ is significantly larger in the FSM case. At the downstream location $z = 7$, the fourth mode even shows the largest

magnitude of all Fourier modes, an indication that an accumulation of energy in the highest azimuthal mode of the calculation occurs. The energy accumulation reveals the lack of resolution or, alternatively, too little model contribution. In general, at $z = 7$, the amplitudes of all modes are strongly reduced versus the DNS case, due to the larger value of the contribution function in this region with larger grid-spacing. Nevertheless, even though the computation was underresolved and the turbulence model contribution was insufficient, the mode shapes show reasonable agreement with the DNS results.

To avoid the aforementioned deficiency of the FSM approach, the grid was refined in order for the calculation to resolve the important scales on the computational grid when they are not removed by the model. Because the resolution in the streamwise direction was significantly coarser than in the DNS and because high-order accurate compact stencils are employed in the radial direction with just 40 points less than in the DNS, it was decided to only increase the streamwise resolution to 392 points with $\Delta z_c = 0.01R$ at the corner (corresponding to the corner resolution of the DNS). The streamwise/radial grid resolution, now not much coarser than for the DNS, in combination with a larger number of Fourier modes approaches the requirements of "traditional" LES, such as Smagorinsky-type LES.

Figure 7 shows the time-averaged streamwise velocity component for $r = 0$ and the averaged pressure coefficient on the base, obtained from FSM calculations on the fine grid for various $\beta$ and different numbers of azimuthal Fourier modes. Choosing $\beta = 1 \times 10^{-3}$, the recirculation length and the base pressure are slightly overpredicted. However, unlike for the coarse grid case, increasing the number of azimuthal Fourier modes from 16 to 32, the same mean base pressure profile is obtained and the streamwise axis-velocity distribution changes only marginally. It also appears as if the dependence of the solution on the constant $\beta$ is not as strong as for the FSM calculation on the coarser grid. When increasing the value of $\beta$ to $4 \times 10^{-3}$, the results are only slightly changed from the cases using $\beta = 1 \times 10^{-3}$ and the best agreement with the DNS results is achieved. Again, when increasing the number of azimuthal Fourier modes from 8 to either 16, or even to 32, the solutions continue to agree well with the DNS results. This implies that the model contribution provided by $f(\Delta/L_K)$ corresponds to what is required for a particular resolution, i.e., the FSM is successful in removing the appropriate amount of energy that cannot be resolved on the respective grid. However, it seems as if this behavior can only be observed if the resolution in none of the spatial directions is overly coarse, .i.e., the gradients of energetic structures cannot be represented. It should also be noted

that the value of $\beta$ which leads to the best agreement with the DNS data is similar to the value that resulted in the best match for lower Reynolds number cases [23,26].

For a more detailed comparison of an FSM calculation on the fine grid with DNS data, the time-averaged radial mode shapes of the streamwise velocity component are shown in Fig. 8. The computation on the fine grid using 32 azimuthal Fourier modes with $\beta = 1 \times 10^{-3}$ was selected, as the contribution function showed values $f(\Delta/L_K) < 5\%$ for the entire computational domain, justifying a classification as (nontraditional) LES. In contrast to the data from the underresolved calculation shown in Fig. 6, bottom, the ratio between the energy of higher azimuthal modes to the first mode is similar to that found for the DNS (Fig. 6, top). In fact, the amplitudes of the higher modes possess smaller values relative to the first mode than in the DNS calculation. As the mode shapes are only shown for the resolved quantities, this implies that the remaining energy of the higher azimuthal modes is provided by the turbulence model, scaled appropriately with the contribution function. The amplitude distributions of most modes agree reasonably well with the mode shapes found with DNS. Merely the first mode, $k = 1$, does not compare well with the DNS data.

To assess whether the FSM succeeds in producing the same kind of coherent structures as those found in the DNS, a vortex-identification method is employed. The $Q$-criterion is named after the second invariant of the gradient of the velocity vector and for compressible flows is computed as $Q = 0.5[(\partial u_i/\partial x_i)^2 + W_{ik}W_{ik} - S_{ik}S_{ik}]$. Instantaneous isocontours of $Q = 0.1$ for the calculation using the fine grid with 32 azimuthal Fourier modes and $\beta = 1 \times 10^{-3}$ are shown in Fig. 9. Qualitatively, similar flow features can be observed as in the DNS, i.e., helical structures within the shear layer, encircling longitudinal structures within the recirculation region. Also, the same type of streamwise structures are present in the trailing wake. However, due to the larger values of the contribution function in this region, and, consequently, an increased amount of turbulence viscosity, a considerably smaller number of small-scale structures appears in the FSM calculation. Nevertheless, considering the good agreement of the mean flow results with the DNS, these small scales seem to be represented reasonably well by the turbulence model.

Overall, the results obtained with the FSM in the URANS-limit show reasonable agreement with the data from the DNS calculation. This is particularly remarkable, considering the drastic savings in computational cost due to the dramatically decreased temporal and spatial resolution requirements as shown in Table 1. Even the computational cost of FSM calculations conducted using the fine grid, which are successful in predicting the same kind of coherent
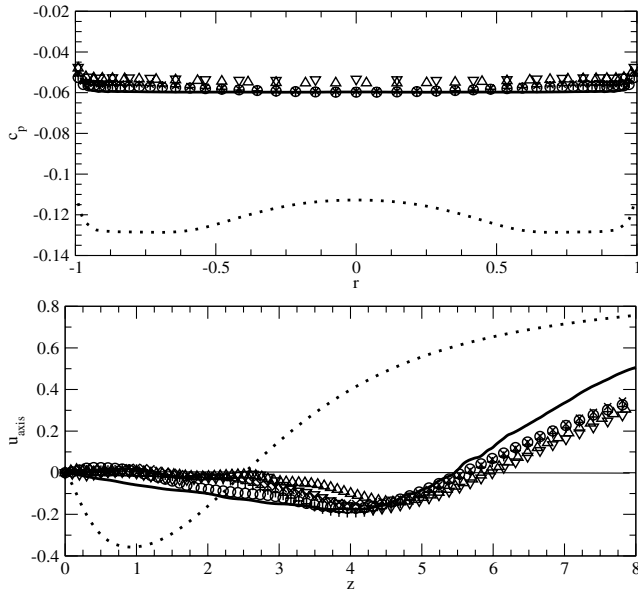


**Fig. 7   Time-averaged base pressure coefficient (top) and streamwise axis velocity (bottom) for FSM calculations on fine grid; DNS, $k_{\max} = 128$ (solid curve), axisymmetric RANS (dotted curve), $\beta = 1 \times 10^{-3}$ and $k_{\max} = 16$ ($\triangle$), $\beta = 1 \times 10^{-3}$ and $k_{\max} = 32$ ($\triangledown$), $\beta = 4 \times 10^{-3}$ and $k_{\max} = 8$ ($\bigcirc$), $\beta = 4 \times 10^{-3}$ and $k_{\max} = 16$ (+), $\beta = 4 \times 10^{-3}$ and $k_{\max} = 16$ ($\times$); $Re_D = 6 \times 10^4$, $M = 2.46$.**
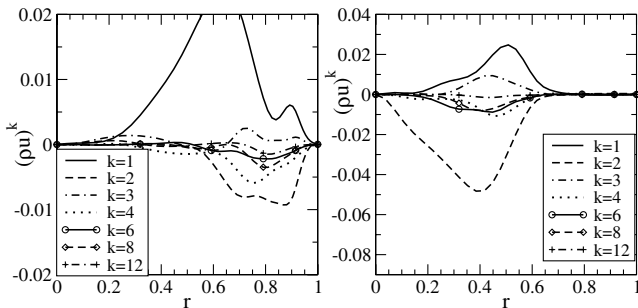


**Fig. 8   Time-averaged mode shapes of $(\rho u)^k$; FSM calculation on fine grid with $k_{\max} = 32$ and $\beta = 1 \times 10^{-3}$; $z = 2.5$ (left) and $z = 7$ (right); $Re_D = 6 \times 10^4$, $M = 2.46$.**



**Fig. 9   Instantaneous isocontours of $Q = 0.1$ for DNS (top) and FSM calculation on fine grid, $k_{\max} = 32$ and $\beta = 1 \times 10^{-3}$ (bottom), perspective view from inflow towards outflow; $Re_D = 6 \times 10^4$, $M = 2.46$.**

**Table 1  Comparison of computational cost per flow-through-time $(t - t_0 \approx 12)$ on HP Alpha of FSM using the coarse computational grid (FSMc), FSM conducted on the fine grid (FSMf) and DNS calculations; $Re_D = 6 \times 10^4$, $M = 2.46$**

| Case | nz | nr | $k_{max}$ | dt | CPU hours |
|------|-----|-----|-----|------|-----------|
| DNS | 812 | 130 | 128 | $1 \times 10^{-3}$ | 759.6[a] |
| FSMc | 194 | 90 | 4 | $2.6 \times 10^{-3}$ | 1.93 |
| FSMc | 194 | 90 | 8 | $2.6 \times 10^{-3}$ | 3.98 |
| FSMc | 194 | 90 | 16 | $2.6 \times 10^{-3}$ | 8.76 |
| FSMf | 392 | 90 | 8 | $2.6 \times 10^{-3}$ | 10.27 |
| FSMf | 392 | 90 | 16 | $2.6 \times 10^{-3}$ | 21.67 |
| FSMf | 392 | 90 | 32 | $1.5 \times 10^{-3}$ | 76.1 |

[a]Computed on SGI Origin 3900, equivalent time on HP Alpha was obtained by dividing the actual CPU hours by five.

structures as observed in the DNS and show better agreement in mean quantities, is still considerably lower than for DNS (c.f., Table 1).

To show that the contribution function $f(\Delta/L_K)$ not only provides the adequate amount of turbulence modeling for varying grid-resolutions (see Figs. 5 and 7), but also when the Reynolds number is changed, several FSM calculations were conducted for $Re_D = 1 \times 10^5$. This was the highest Reynolds number for which DNS data was available [6]. The setup of the FSM calculations follows the FSM calculations of the $Re_D = 6 \times 10^4$ cases on the coarse grid. It has been shown that at this Reynolds number azimuthal modes up to $k = 16$ contain a considerable amount of energy [6]. Hence, FSM calculations with $k_{max} = 16$ were conducted. The time-averaged pressure coefficient and streamwise axis-velocity are shown in Fig. 10. As for the FSM calculations at lower Reynolds numbers, best agreement with the DNS data is achieved when choosing $\beta = 2 \times 10^{-3}$ or $\beta = 4 \times 10^{-3}$. An entirely flat pressure distribution on the base is predicted with the correct mean value and the recirculation length agrees very well with that obtained using DNS. The reduction in computational time for this case is even more dramatic than for the lower Reynolds number case, as the DNS calculation required an increased number of grid points and, consequently, smaller time steps. Because the FSM calculations were conducted on the same computational grids as that used for the $Re_D = 6 \times 10^4$ case, the computational cost did not increase and is listed in the fourth row of Table 1. The preceding results illustrate, that on a given computational grid, the contribution function, using

the same values of $\beta$, successfully provides the appropriate amount of turbulence modeling for varying Reynolds numbers.

### B.  High Reynolds Number Wakes

So far, FSM was shown to reproduce DNS results of transitional axisymmetric wakes with reasonable accuracy at significantly lower computational cost. However, most applications that involve base flows, such as projectiles or coasting missiles, are subject to considerably higher Reynolds numbers. Experimental results of high Reynolds number wakes ($Re_D = 3.3 \times 10^6$) at $M = 2.46$ by Dutton and coworkers at UIUC will be used for reference and are denoted as "UIUC case" in the following. The flow investigated in the experiments is fully turbulent, i.e., a turbulent approach flow separates at the base corner and the shear layer that forms immediately downstream of the base also is turbulent.

To significantly reduce the computational cost of the simulations, the following setup was applied to all calculations: a precursor RANS calculation of the approach boundary layer was conducted with $\Delta r^+ = 0.8$ that showed very good agreement with the experimental data [30]. The approach boundary layer data was interpolated onto the (coarser) radial grid of the full base flow calculation and fixed, i.e., the approach flow remained unchanged throughout the simulations.

This approach is considerably different from what other researchers have attempted, such as full LES of the inflow [14]. However, the concept is not unlike the procedure inherent in the DES approach, where the wall-bounded flow region is represented by a steady RANS solution [18,19]. Several aspects appear to justify this procedure for the present case: the approach boundary layer is thin relative to the radius of the base ($\delta_c = 0.1$), thereby most likely not introducing significant (low frequency) unsteadiness into the initial shear layer. Furthermore, with the flow being supersonic and an expansion wave forming at separation, no significant feedback from the recirculation region with the approach flow is expected. This is supported by pressure measurements in the approach boundary layer which showed that no upstream influence from the base corner separation was evident in the data [3].

#### 1.  Axisymmetric RANS Calculations

Axisymmetric RANS calculations of the UIUC case were performed to evaluate their performance for a fully turbulent base flow and serving as initial conditions for FSM computations. Several computational grids were used for the RANS calculations to determine the grid dependence of the turbulence closure. The coarsest grid had 210 points in the radial direction and 256 points in the streamwise direction, with the smallest grid spacing at the base corner being $\Delta r_c = \Delta z_c = 5 \times 10^{-3}$. The finest grid used contained 350 and 512 points in the radial and the streamwise directions, respectively, with $\Delta r_c = \Delta z_c = 4 \times 10^{-4}$.

For all calculations employing the $EASM_\alpha$, the wall-distance independent version with $c_T = 4.45$ was used [30]. For reference, axisymmetric RANS calculations employing the STKE model were conducted. Figure 11 shows the streamwise axis-velocity and the radial distributions of the pressure coefficient $c_p$ on the base obtained from several axisymmetric RANS calculations. The data from the experiments conducted at UIUC are included for comparison. Only results from calculations using the coarse grid are presented, as they showed no difference from the calculations performed on the fine grid, implying that the grid resolution was adequate. Consistent with all previous axisymmetric results, the base pressure distribution displays a significant radial variation, which is not present in the experimental data. It can be observed that the calculations employing the $EASM_\alpha$ overpredict the recirculation length significantly, resulting in too high a pressure at the base. When the STKE closure is used, the recirculation length is slightly shorter; however, the base pressure is underpredicted.

The calculations were repeated omitting the compressible extensions (c.e.) added to the source terms $\Pi^R$, $\Pi_K$, and $\Pi_\epsilon$, which reduce the turbulence production, and it can be seen in Fig. 11 (bottom) that the recirculation length is reduced. In fact, the STKE
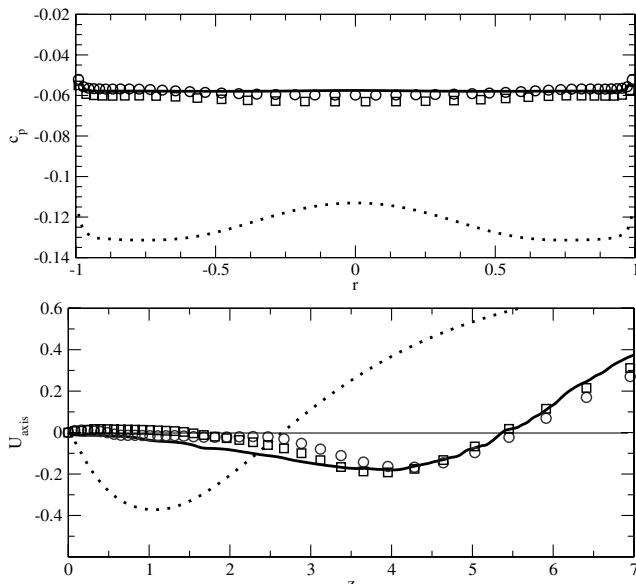
**Fig. 10  Time-averaged base pressure coefficient (top) and streamwise axis velocity (bottom) for FSM calculations on coarse grid with $k_{max} = 16$; DNS, $k_{max} = 128$ (solid curve), axisymmetric RANS (dotted curve), $\beta = 2 \times 10^{-3}$ (◯), $\beta = 4 \times 10^{-3}$ (□); $Re_D = 1 \times 10^5$, $M = 2.46$.**
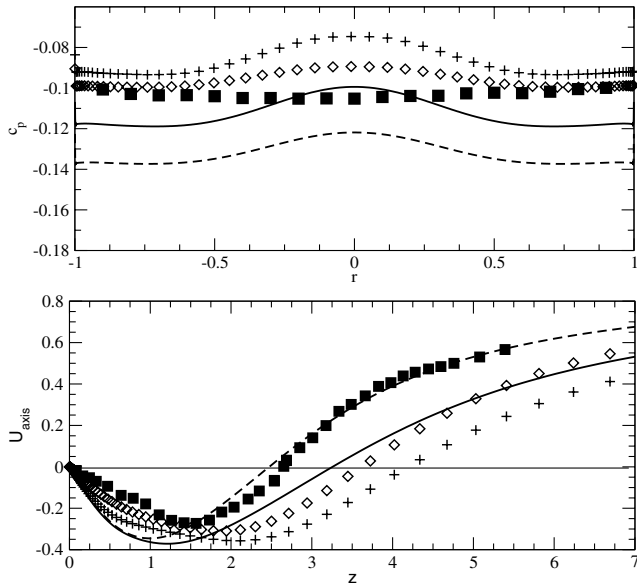
**Fig. 11** Base pressure coefficient (top) and streamwise axis velocity (bottom) obtained from axisymmetric RANS calculations; UIUC case (■), STKE using c.e. (solid curve), STKE omitting c.e. (dashed curve), EASM$_\alpha$ using c.e. (+), EASM$_\alpha$ omitting c.e. (◇); $Re_D = 3.3 \times 10^6$, $M = 2.46$.



**Fig. 12** Radial profiles of $u$, $v$, $K$, and $\langle u'v' \rangle$ from axisymmetric RANS calculations; experiments at UIUC (■), STKE using c.e. (solid curve), STKE omitting c.e. (dashed curve), EASM$_\alpha$ using c.e. (+), EASM$_\alpha$ omitting c.e. (◇); $z = 0.078$ (top), $z = 2.67$ (bottom); $Re_D = 3.3 \times 10^6$, $M = 2.46$.

model solution shows quite good agreement with the experiment in terms of recirculation length. However, the reverse flow maximum is too large and the base pressure is underpredicted even more strongly than when including c.e. The solution obtained with the EASM$_\alpha$ also shows a reduction in the recirculation length and a decrease in mean base pressure when omitting the c.e., albeit the effect is not as pronounced as when the STKE model is used.

To get a more complete picture of the solutions predicted with the axisymmetric RANS calculations, radial profiles of the streamwise and radial velocity components, $K$ and the dominant Reynolds shear-stress component $\langle u'v' \rangle$ are shown in Fig. 12 for two streamwise locations at which experimental data was available. At the streamwise location closest to the base, $z = 0.078$, the velocity profiles obtained numerically show reasonable agreement with the experimental data. However, the maximum $K$ value in the shear layer is underpredicted by all turbulence closures, most severely when using the EASM$_\alpha$. In addition, the EASM$_\alpha$ also predicts too low values of $K$ within the recirculation region. The distribution of the Reynolds shear stress $\langle u'v' \rangle$ is predicted reasonably well; however, the measured peak value in the shear layer is not reached by any of the RANS calculations. At the mean reattachment point $z = 2.67$, reverse flow is predicted at the axis with all turbulent closures due to the overprediction of the recirculation length, shown in Fig. 12, except when using the STKE omitting the c.e. The EASM$_\alpha$ significantly underpredicts $K$, regardless of wether the c.e. are used or not. In contrast, the level of $K$ has increased to values comparable to the experimental data when employing the STKE model including the c.e. $K$ is even considerably overpredicted when neglecting the compressibility modifications. Reasonable agreement with the experiments in terms of the Reynolds shear stress is also found when using the turbulence closures without c.e. The preceding observations lead to the conclusion that the $K$ level at the inflow might not be sufficiently large. For that reason, the value of $K$ was rescaled by a factor of 6 to correspond with the data by Dutton and coworkers at the streamwise position $z = 0.078$. A separate boundary layer calculation was conducted prescribing this new value of $K$ and epsilon was left to adjust in order to satisfy the transport equations (a slight change in the velocity components was unavoidable). The authors recognize that such a rescaling is certainly not desired for the calculation of practical flows, in particular when considering RANS and FSM as predictive methods. However, here it serves the purpose of demonstrating the importance of the inflow conditions on the entire solution and still permits comparison between various
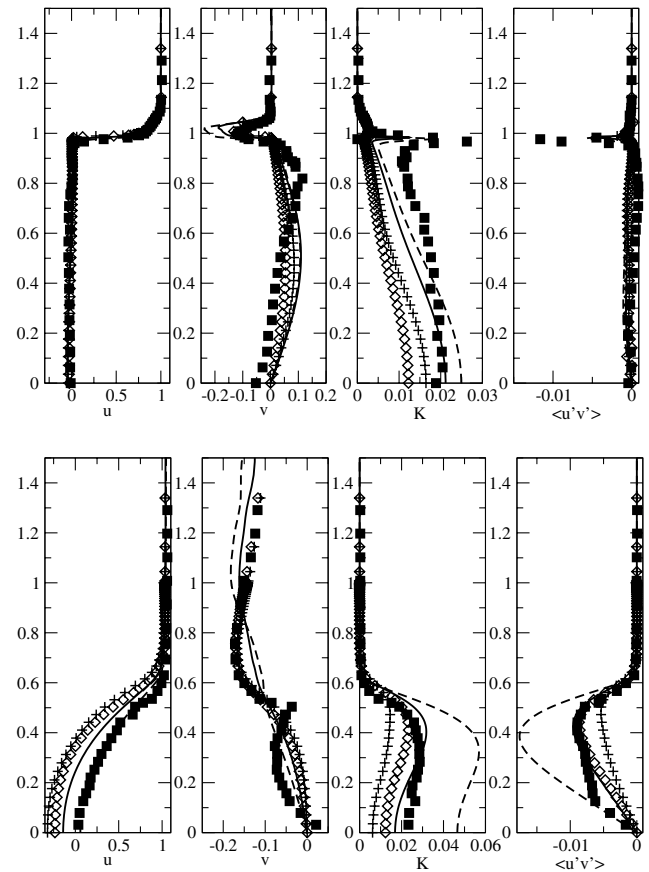
calculations using the same inflow conditions. Axisymmetric RANS calculations, employing both the EASM$_\alpha$ and the STKE model, were repeated using the changed inflow.

In addition to the modified approach-flow conditions, the effect of altering several coefficients in the turbulence closures were investigated. Papp et al. [31] recognized that the EASM$_\alpha$ was calibrated for homogeneous turbulent wall-bounded flows, leading to an underprediction of mixing rates in shear layers. They therefore made an attempt to recalibrate the EASM$_\alpha$ for high Reynolds number jet flows and determined that an increase of $a_1$ from 0.4866 to 0.5416 had the desired effect of increasing the turbulence levels in the shear layer without adversely affecting the pressure-strain rate correlation. In addition, $C_{\epsilon 1} = 1.43$ and $C_{\epsilon 2} = 1.92$ were used as they were specifically calibrated for high Reynolds number jet flows [32]. The similarities between the base flow and jets, such as a mean streamwise velocity profile featuring two inflection points might suggest that the coefficients calibrated for jets might also be applicable to base flows. Calculations employing this new set of constants are denoted by "Papp" in the following.

Results obtained from the axisymmetric RANS calculations investigating the influence of various coefficients in the turbulence closures and using rescaled inflow values for $K$ and $\epsilon$ are presented in Fig. 13. The calculation employing the EASM$_\alpha$ with the original coefficients and using c.e. is the only case that was also conducted for the original inflow conditions, presented in Fig. 11. The effect of the significantly increased levels of $K$ and $\epsilon$ in the approach flow is a drastic decrease in recirculation length and, consequently, base pressure. When the coefficients in the EASM$_\alpha$ closure are changed to the values suggested by Papp et al. [31], the recirculation length is further decreased and the mean reattachment point corresponds well with the experimental data when the c.e. are included.
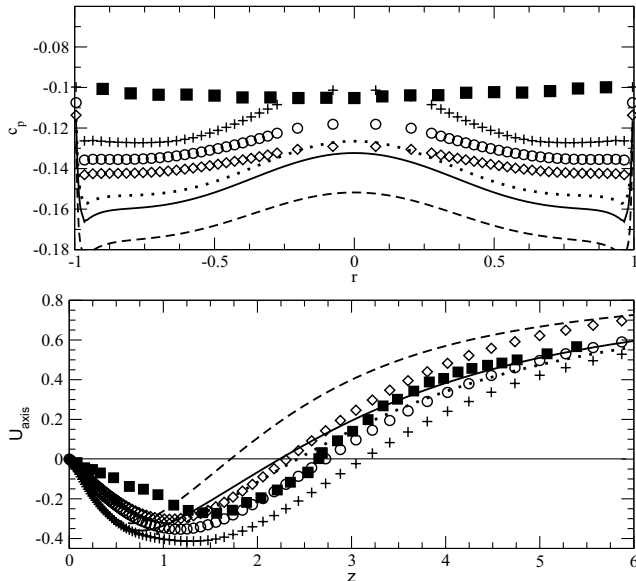
**Fig. 13  Base pressure coefficient (top) and streamwise axis velocity (bottom) obtained from axisymmetric RANS calculations with modified inflow: UIUC case (■); STKE using c.e. and $C_{\epsilon 1} = 1.44$, $C_{\epsilon 2} = 1.88$ (dotted curve); STKE using c.e. and $C_{\epsilon 1} = 1.43, C_{\epsilon 2} = 1.92$ (solid curve); STKE omitting c.e. and $C_{\epsilon 1} = 1.43, C_{\epsilon 2} = 1.92$ (dashed curve); $EASM_\alpha$ using c.e. and original coefficients (+); $EASM_\alpha$ using c.e. and coefficients according to Papp et al. [31] (○); $EASM_\alpha$ omitting c.e. and coefficients according to Papp et al. (◇); $Re_D = 3.3 \times 10^6$, $M = 2.46$.**

The base pressure, however, is also further decreased and therefore underpredicts the reference data even more strongly, in particular when the compressibility extensions are not included. All calculations that were conducted with the STKE model underpredicted both the recirculation length and the base pressure significantly, especially when choosing $C_{\epsilon 1} = 1.43$ and $C_{\epsilon 2} = 1.92$.

Radial profiles of the streamwise and radial velocity components, $K$ and $\langle u'v' \rangle$, are shown for the cases with the modified inflow in Fig. 14. Three streamwise locations are selected, one immediately downstream of separation, one within the recirculation region, and one at the mean reattachment point in the experiments. At the streamwise location closest to the base, $z = 0.078$, the velocity profiles obtained numerically show good agreement with the experimental data. In contrast to the results discussed earlier, the distribution of $K$ corresponds well with the experimental data when using the $EASM_\alpha$. The STKE closure overpredicts $K$ at this location. The Reynolds shear stress obtained from all RANS calculations shows good agreement with the experimental data. When looking at the profiles obtained within the recirculation region, at $z = 1.26$, it can be observed that the STKE model severely overpredicts $K$ and the Reynolds shear stress. Quite good agreement with the experimental data is found for the turbulence quantities when employing the $EASM_\alpha$ with the modification according to Papp et al. [31]. Using the original coefficients for the $EASM_\alpha$, both $K$ and $\langle u'v' \rangle$ are underpredicted. The converse, however, is the case for locations farther downstream. At the location $z = 2.67$, best agreement with the experimental data for the turbulence quantities is found when using the $EASM_\alpha$ with the original coefficients. The recalibrated $EASM_\alpha$ overpredicts both $K$ and $\langle u'v' \rangle$ at the mean reattachment point. At the latter location, the STKE model considerably overpredicts the maxima of both $K$ and $\langle u'v' \rangle$.

Overall, choosing $c_{\epsilon 1} = 1.43$ and $c_{\epsilon 2} = 1.92$ and using the modifications to the $EASM_\alpha$ suggested by Papp et al. [31] leads to an increase in $K$ and the Reynolds shear stress, causing a decrease in recirculation length and base pressure. Conversely, incorporating c. e. results in decreased values of $K$ and $\langle u'v' \rangle$ and, consequently, an increase in recirculation length and base pressure. The inflow values for the turbulent quantities $K$ and $\epsilon$ are shown to play a significant role in the global solution. Larger values of $K$ and $\epsilon$ at the inflow produce a smaller base pressure and a reduced recirculation length. In
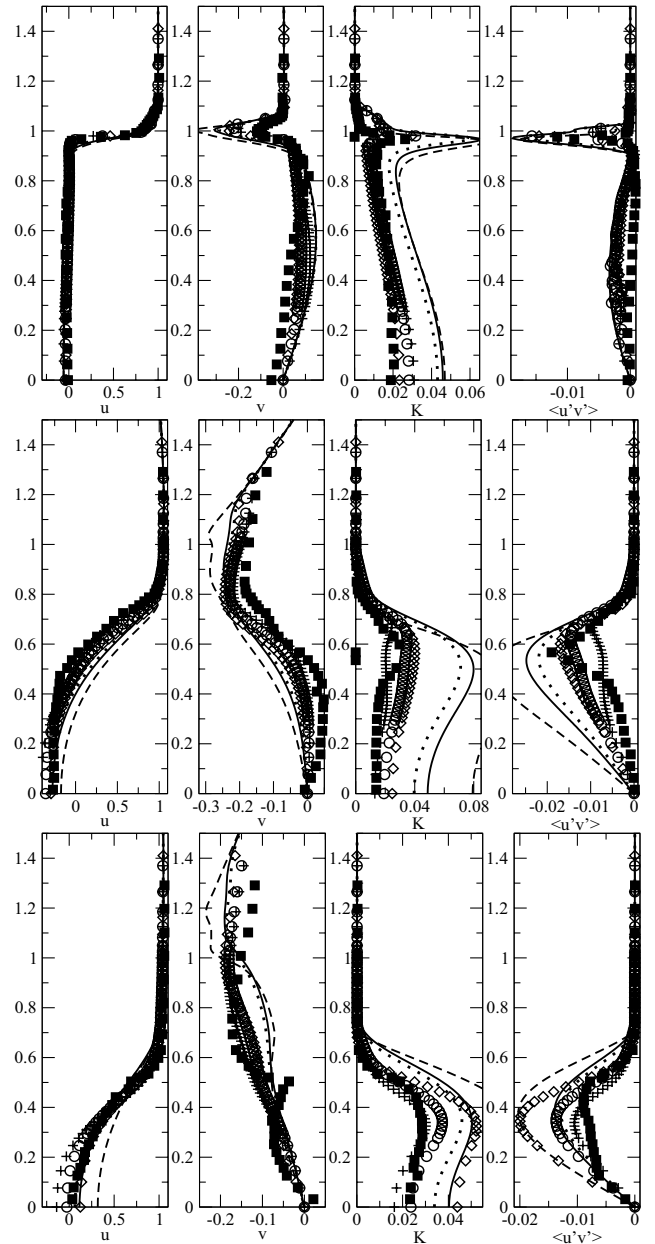


**Fig. 14   Radial profiles of $u$, $v$, $K$, and $\langle u'v' \rangle$ from RANS calculations using modified inflow conditions: experiments at UIUC (■); STKE using c.e. and $C_{\epsilon 1} = 1.44$, $C_{\epsilon 2} = 1.88$ (dotted curve); STKE using c.e. and $C_{\epsilon 1} = 1.43, C_{\epsilon 2} = 1.92$ (solid curve); STKE omitting c.e. and $C_{\epsilon 1} = 1.43, C_{\epsilon 2} = 1.92$ (dashed curve); $EASM_\alpha$ using c.e. and original coefficients (+); $EASM_\alpha$ using c.e. and coefficients according to Papp et al. [31] (○); $EASM_\alpha$ omitting c.e. and coefficients according to Papp et al. (◇); from top to bottom $z = 0.078$, $z = 1.26$, and $z = 2.67$; $Re_D = 3.3 \times 10^6$, $M = 2.46$.**

general, the $EASM_\alpha$ appears to produce more accurate distributions of turbulence quantities and a flatter base pressure distribution. However, none of the RANS calculations is able to reproduce the UIUC results accurately, implying that it is essential to capture the unsteady dynamics of the large-scale structures, as was already demonstrated for the transitional cases.

### 2.   3-D FSM Calculations

Considering the results obtained from the axisymmetric RANS calculations, all FSM calculations of the UIUC case were conducted employing the $EASM_\alpha$ using compressible extensions and coefficients according to Papp et al. [31]. The axisymmetric RANS data was used as initial condition and the desired number of

azimuthal Fourier modes was added. Initially, the same constant $\beta$ was employed as for all transitional cases. However, even with the finest grid resolution used in the $r$–$z$-plane and up to 32 azimuthal Fourier modes, the contribution function was on the order of 40%. Such a large amount of model contribution did not permit the formation of structures. Thus, to reduce the magnitude of the contribution function sufficiently to allow for the generation and evolution of structures in the flow, a significantly finer grid would have been required leading to very high computational cost with the currently used explicit time integration. Instead, $\beta$ was decreased to values of the order of $\mathcal{O}(10^{-4})$. This resulted in $f(\Delta/L_K) < 10\%$ in the initial shear layer and within the recirculation region, and increasing values in the trailing wake due to the strong streamwise stretching of the grid. However, it would be desirable to repeat the simulations with considerably increased grid resolution to achieve $f(\Delta/L_K) < 10\%$ in the initial shear layer and within the recirculation region employing the same values of $\beta$ as for the transitional cases. The required resolution can be determined a priori once $L_K$ is known from an axisymmetric RANS.

FSM calculations were conducted on the coarse grid presented for the axisymmetric RANS calculations and on a grid composed of the same radial distribution as the coarse grid, but with a refined grid in the streamwise direction. In the experiments conducted at UIUC, longitudinal structures were observed within the shear layer. To capture streamwise structures within the initial shear layer, it was determined that at least 16 azimuthal Fourier modes were required. Therefore, the FSM calculations were exclusively conducted with $k_{\max} \geq 16$.

A time sequence of instantaneous isocontours of $Q = 0.5$, obtained from the FSM calculation using the refined grid, and 16 azimuthal Fourier modes are presented in Fig. 15. The time difference between each consecutive time level is $\Delta t = 1$, which corresponds to freestream fluid traveling one base-radius downstream. Helical structures in the shear layer can clearly be identified which travel downstream (see, e.g., structures marked with "A" or "C"). The high-wavenumber variation of the helical structures most likely is caused by streamwise structures in the shear layer, as observed in endviews of the experimental data and DNS data at $Re_D = 1 \times 10^5$ [6]. As in the transitional cases, streamwise structures are present within the recirculation region and extend into the developing wake. The structures vanish downstream of the mean reattachment point due to the large contribution of the turbulence model. A distinction from the transitional cases is the formation of hairpin vortices, as marked with "B," upstream of the recompression region. These might be generated by secondary instabilities affecting the initial helical structures in the shear layer. Alternatively, they could be produced by fluid forming streamwise structures when passing the chevronlike structure of the inner shear layer [7].

To evaluate whether the FSM calculations are capable of reproducing the mean flow data available from the experiments, the base pressure distribution and the streamwise axis-velocity are presented in Fig. 16. As opposed to the RANS solution, shown for comparison, $c_p$ obtained from the FSM calculations show good agreement with the experimental curve, in particular considering the radial distribution. The mean pressure value depends on the grid resolution of the respective calculation. Both calculations employing $k_{\max} = 16$ show the smallest deviation from the experimental data. For the calculation on the fine grid, using 32 azimuthal Fourier modes, the pressure value is slightly underpredicted. In spite of the good results obtained for the pressure distribution, all FSM calculation overpredict the recirculation length by approximately 0.7 radii. Several reasons for this behavior are suggested: first, the values of $K$ and $\epsilon$ in the (fixed) approach flow might not correspond to those present in the experiments. It was shown with the preceding axisymmetric RANS calculations that the magnitudes of the turbulent quantities at the inflow have a pronounced effect on the global solution, in particular on the recirculation length. Second, a very small value of $\beta$ was chosen for a grid that most likely was too coarse to resolve the relevant length scales (see discussion of transitional cases). Third, a steady approach boundary layer is prescribed, and, therefore, the generation of unsteadiness is delayed,
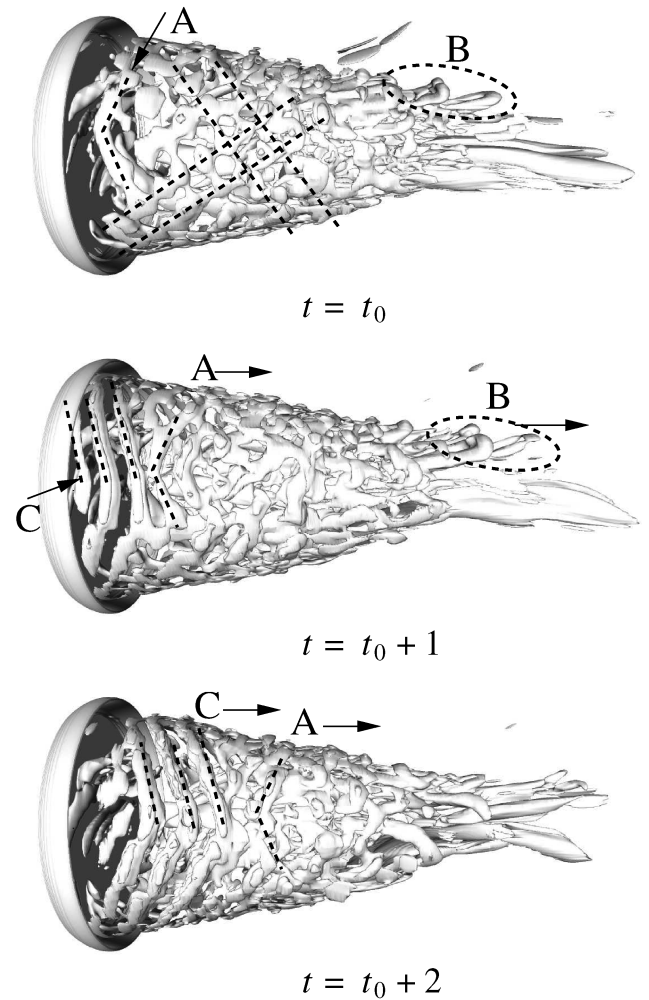


**Fig. 15** Instantaneous isocontours of $Q = 0.5$ for FSM calculation using $k_{\max} = 16$ and $\beta = 1 \times 10^{-4}$, perspective side views with flow from left to right, base of body shaded dark gray; $Re_D = 3.3 \times 10^6$, $M = 2.46$.
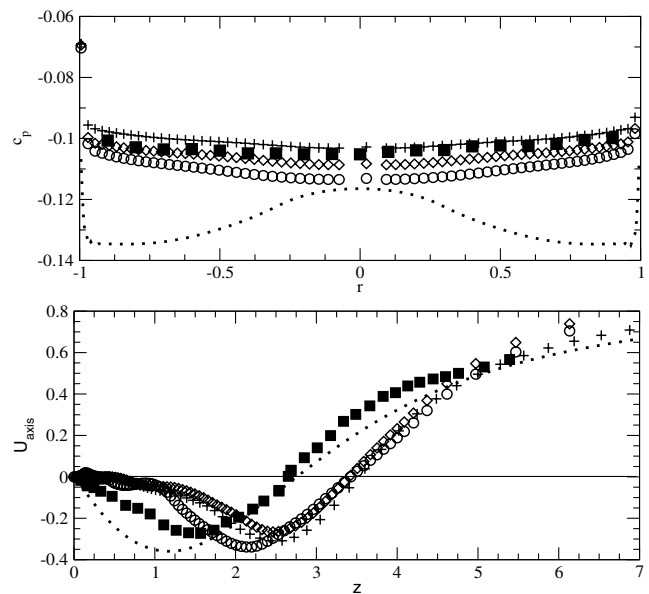


**Fig. 16** Time-averaged pressure coefficient on base (top) and streamwise velocity along axis of symmetry (bottom) obtained from FSM calculations; UIUC case (■), axisymmetric RANS calculation (dotted line), FSM with 256 streamwise points, $\beta = 1 \times 10^{-4}$ and $k_{\max} = 16$ (+), FSM with 512 streamwise points, $\beta = 1 \times 10^{-4}$ and $k_{\max} = 16$ (◇), FSM with 512 streamwise points, $\beta = 1 \times 10^{-4}$ and $k_{\max} = 32$ (○); $Re_D = 3.3 \times 10^6$, $M = 2.46$.

i.e., the flow must "transition" from a steady to an unsteady state downstream of the base. The shallow slopes of the streamwise axis-velocity profiles might be an indication that this is indeed the case. The slopes resemble those found for all transitional cases from both DNS and FSM calculations. In the fully turbulent UIUC case, the slope at the base-wall is considerably steeper. All axisymmetric RANS calculations produce an even larger slope, presumably because turbulence production is overpredicted in this region.

## VI.  Summary

Axisymmetric RANS and three-dimensional FSM calculations were conducted of transitional and fully turbulent supersonic base flows. In all cases, axisymmetric RANS calculations failed to accurately reproduce the DNS or experimental data, indicating that relevant physical mechanisms could not be captured. A strong radial variation of the base pressure was predicted by all closures, and, for most cases, the recirculation length was underpredicted. Overall, the $EASM_\alpha$ appears to be the best closure of the ones considered for the calculation of supersonic base flows. It was demonstrated that the values of the turbulent quantities $K$ and $\epsilon$ at the inflow have a strong impact on the global RANS solution, with larger levels of $K$ leading to a smaller base pressure and a decreased recirculation length. Compressible extensions were shown to decrease the turbulence levels in the shear layer, whereas the choice of model coefficients suggested by Papp et al. [31] increased turbulence levels.

For all transitional cases, FSM is capable of reproducing the DNS data with reasonable accuracy at a fraction of the computational cost. The optimal value of the parameter in the contribution function appears to be $1 \times 10^{-3} \leq \beta \leq 4 \times 10^{-3}$ for all transitional Reynolds numbers. For a constant value of $\beta$, the grid resolution in the azimuthal direction can be significantly increased, maintaining the same correct solution. This implies that the FSM strategy successfully removes the appropriate amount of energy from the calculations that cannot be resolved on the respective grid. FSM calculations with only four azimuthal Fourier modes confirmed that the low wavenumber modes are responsible for a flat base pressure distribution.

It was shown that the FSM approach is not derived for a specific turbulence model but is a general strategy for solving unsteady, three-dimensional flows. FSM appears to sufficiently scale down the model contribution in the relevant regions so as not to inhibit the physical instability mechanisms responsible for the generation of large structures. The same kind of structures in the flowfield are predicted by FSM calculations as by DNS, i.e., mainly helical structures in the shear layer and streamwise structures within the recirculations region and in the trailing wake.

FSM calculations of a fully turbulent case show good agreement with the UIUC experiments in terms of the base pressure. Nevertheless, the recirculation length is overpredicted, most likely due to the use of a steady approach boundary layer and the values of $K$ and $\epsilon$ not corresponding to those present in the experiments. Note also that to limit computational cost the value of $\beta$ was chosen an order of magnitude smaller than for the transitional cases to allow for the generation of large-scale structures. However, the authors believe that $1 \times 10^{-3} \leq \beta \leq 4 \times 10^{-3}$ is also appropriate for the high Reynolds number if the grid resolution is increased such that the contribution function $f(\Delta/L_K) < 10\%$ in the relevant regions.

The simulations at high Reynolds number revealed structures similar to those found in DNS of transitional wakes [7]: helical structures in the shear layer with a strong azimuthal modulation caused by higher azimuthal modes, and a significant number of streamwise structures within the recirculation region. In addition, the formation of hairpin vortices upstream of the recompression region was detected.

## Acknowledgments

## References

[1] Rollstin, L., "Measurement of Inflight Base-Pressure on an Artillery-Fired Projectile," *Journal of Spacecraft and Rockets*, Vol. 27, No. 1, 1990, pp. 5–6.

[2] Herrin, J. L., and Dutton, J. C., "An Experimental Investigation of the Supersonic Axisymmetric Base Flow Behind a Cylindrical Afterbody," UILU 91-4004, University of Illinois at Urbana–Champaign, 1991.

[3] Herrin, J. L., and Dutton, J. C., "Supersonic Base Flow Experiments in the Near Wake of a Cylindrical Afterbody," *AIAA Journal*, Vol. 32, No. 1, 1994, pp. 77–83.

[4] Bourdon, C. J., and Dutton, J. C., "Planar Visualizations of Large-Scale Turbulent Structures in Axisymmetric Supersonic Separated Flows," *Physics of Fluids*, Vol. 11, No. 1, 1999, pp. 201–213.

[5] Herrin, J. L., and Dutton, J. C., "Supersonic Near-Wake Afterbody Boattailing Effects on Axisymmetric Bodies," *Journal of Spacecraft and Rockets*, Vol. 31, No. 6, 1994, pp. 1021–1028.

[6] Sandberg, R. D., and Fasel, H. F., "Direct Numerical Simulations of Transitional Supersonic Base Flows," *AIAA Journal*, Vol. 44, No. 4, 2006, pp. 848–858.

[7] Sandberg, R. D., and Fasel, H. F., "Numerical Investigation of Transitional Supersonic Axisymmetric Wakes," *Journal of Fluid Mechanics*, 2006 (in press).

[8] Sahu, J., Nietubicz, C., and Steger, J., "Navier-Stokes Computations of Projectile Base Flow with and Without Mass Injection," *AIAA Journal*, Vol. 23, No. 9, 1985, pp. 1348–1355.

[9] Sahu, J., "Numerical Computations of Supersonic Base Flow with Special Emphasis on Turbulence Modeling," *AIAA Journal*, Vol. 32, No. 7, 1992, pp. 1547–1549.

[10] Tucker, P., and Shyy, W., "A Numerical Analysis of Supersonic Flow over an Axisymmetric Afterbody," AIAA Paper 93-2347, 1993.

[11] Krishnamurty, V. S., and Shyy, W., "Study of Compressibility Modifications to the $k$–$\epsilon$ Tturbulence Model," *Physics of Fluids*, Vol. 9, No. 9, 1997, pp. 2769–2788.

[12] Sarkar, S., Erlebacher, G., Hussaini, M. Y., and Kreiss, H. O., "The Analysis and Modelling of Dilatational Terms in Compressible Turbulence," *Journal of Fluid Mechanics*, Vol. 227, June 1991, pp. 473–493.

[13] Sarkar, S., "The Pressure-Dilatation Correlation in Compressible Flows," *Physics of Fluids A*, Vol. 4, No. 12, 1992, pp. 2674–2682.

[14] Fureby, C., "Large Eddy Simulation of Supersonic Baseflow," AIAA Paper 99-0426, 1999.

[15] Speziale, C. G., "A Combined Large-Eddy Simulation and Time-Dependent RANS Capability for High-Speed Compressible Flows," Boston Univ., Tech. Rept. AM-97-022, Boston, 1997.

[16] Jiménez, J., and Moser, R. D., "LES: Where are We and What Can We Expect," AIAA Paper 98–2891, 1998.

[17] Spalart, P. R., Jou, W.-H., Strelets, M., and Allmaras, S. R., "Comments on the Feasibility of LES for Wings, and on a Hybrid RANS/LES Approach," *Advances in DNS/LES, 1st AFOSR International Conference on DNS/LES*, Greyden Press, Columbus, OH, 1997, p. 137.

[18] Forsythe, J. R., and Hoffmann, K. A., "Detached-Eddy Simulation of a Supersonic Axisymmetric Base Flow with an Unstructured Solver," AIAA Paper 2000-2410, June 2000.

[19] Forsythe, J. R., Hoffmann, K. A., and Squires, K. D., "Detached-Eddy Simulation with Compressibility Corrections Applied to a Supersonic Axisymmetric Base Flow," AIAA Paper 2002-0586, Jan. 2002.

[20] Speziale, C. G., "Turbulence Modeling for Time-Dependent RANS and VLES: A Review," *AIAA Journal*, Vol. 36, No. 2, 1998, pp. 173–184.

[21] Speziale, C. G., "A Combined Large-Eddy Simulation and Time-Dependent RANS Capability for High-Speed Compressible Flows," *Journal of Scientific Computing*, Vol. 13, No. 3, 1998, pp. 253–74.

[22] Fasel, H. F., Seidel, J. J., and Wernz, S. H., "A Methodology for Simulation of Complex Turbulent Flows," *Journal of Fluids Engineering*, Vol. 124, No. 4, 2002, pp. 933–942.

[23] Fasel, H. F., Von Terzi, D. A., and Sandberg, R. D., "A Methodology for Simulating Compressible Turbulent Flows," *Journal of Applied Mechanics*, Vol. 73, No. 3, 2006, pp. 405–412.

[24] Rumsey, C. L., Gatski, T. B., and Morrison, J. H., "Turbulence Model Predictions of Strongly Curved Flow in a U-Duct," *AIAA Journal*, Vol. 38, No. 8, 2000, pp. 1394–1402.

[25] Gatski, T. B., and Speziale, C. G., "On Explicit Algebraic Stress Models for Complex Turbulent Flows," *Journal of Fluid Mechanics*, Vol. 254, Sept. 1993, pp. 59–78.

[26] Sandberg, R. D., and Fasel, H., "A Flow Simulation Methodology for Compressible Turbulent Axisymmetric Wakes," AIAA Paper 2003-0267, Jan. 2003.

[27] Rumsey, C. L., and Gatski, T. B., "Recent Turbulence Model Advances Applied to Multielement Airfoil Computations," *Journal of Aircraft*, Vol. 38, No. 5, 2001, pp. 904–910.

[28] Gottlieb, D., and Turkel, E., "Dissipative Two-Four Methods for Time-Dependent Problems," *Mathematics of Computation*, Vol. 30, No. 136, 1976, pp. 703–723.

[29] Sandberg, R. D., "Numerical Investigation of Transitional and Turbulent Supersonic Axisymmetric Wakes," Ph.D. Thesis, Univ. of Arizona, Tucson, AZ, Dec. 2004.

[30] Sandberg, R. D., and Fasel, H., "Application of a New Flow Simulation Methodology for Supersonic Axisymmetric Wakes," AIAA Paper 2004-0067, Jan. 2004.

[31] Papp, J., Kenzakowski, D., and Dash, S., "Calibration and Validation of EASM Turbulence Model for Jet Flowfields," AIAA Paper 2002-0855, Jan. 2002.

[32] Launder, B. E., and Sharma, B. I., "Application of the Energy-Dissipation Model of Turbulence to the Calculation of Flow Near a Spinning Disc," *Letters in Heat and Mass Transfer*, Vol. 1, Nov.–Dec. 1974, pp. 131–138.

X. Zhong
*Associate Editor*